Physical Controls on the Shape of Earthquake Source Time Functions

Cheng-Yi Wang[1] and Chun-Yu Ke[1]

[1]Department of Civil Engineering, National Taiwan University, Taipei, Taiwan

Key Points:

- Rupture initiation location and fault geometry control STF growth and plateau, while stress gradient and friction govern arrest behavior.
- Long-tailed STFs can arise from weakening over a slip distance comparable to total slip, supporting scale-dependent breakdown.
- Initiation location, patch geometry, stress gradient, and frictional weakening act on largely separable STF features.

Corresponding author: Chun-Yu Ke, `chunyuke@ntu.edu.tw`

Abstract

The earthquake source time function (STF), i.e., the seismic moment rate function, is a key observable of source dynamics, yet the physical origins of its diverse shapes, spanning sub-quadratic to super-quadratic growth, symmetric to asymmetric peaks, and abrupt to long-tailed decays, remain incompletely understood. Prior studies examined rupture initiation location, fault geometry, stress distribution, and frictional weakening individually, but not their combined effects on STF shape. Using spectral boundary-integral simulations of idealized overstressed-patch configurations, we show that four physical mechanisms each govern a distinct STF feature. Initiation location controls growth-phase curvature and symmetry, shifting moment rate growth from quadratic to nearly linear as rupture becomes increasingly unilateral. The background stress gradient acts almost exclusively on the arrest phase, with steeper gradients producing more abrupt termination, while overstress zone geometry governs plateau development and produces pulse-like slip without explicit self-healing. None of these structural controls reproduces the strongly early-peaking, long-tailed STF shapes common in natural earthquakes. Pronounced long-tailed behavior emerges only when the secondary frictional weakening distance is comparable to or exceeds total fault slip, consistent with scale-dependent breakdown. Combined simulations pairing initiation location with stress gradient and frictional weakening show the controls to be largely separable, though not additive in peak timing, so much of the diversity of observed STF shapes can arise from combinations of these mechanisms and heterogeneity-based processes not examined here. These findings provide an improved physical basis for interpreting STFs, with implications for seismic source inversion and near-fault ground motion prediction.

Plain Language Summary

When an earthquake occurs, the fault does not release all of its energy at once. Instead, the energy builds up as the rupture spreads and then tapers off as the rupture stops. This energy-release history differs greatly from one earthquake to another, and scientists have long wondered what controls these differences. We used numerical simulations to test how four factors affect this history: where the rupture starts, how abruptly stress in the surrounding rock drops off, the shape of the stressed region on the fault, and how the fault surface loses strength as it slides. Each factor controls a different part of this history in a predictable way. However, none of the first three factors explains the slowly fading energy release seen in many large earthquakes. That slow fading appears only when the fault keeps losing strength over a sliding distance as large as the earthquake's total slip, suggesting a more extended and gradual weakening process than simple friction models describe. Because these factors work largely independently, their combinations can explain much of the variety of energy-release histories seen in real earthquakes, helping scientists better interpret seismic recordings and assess earthquake hazards.

1 Introduction

The source time function (STF), i.e., the seismic moment rate function $\dot{M}_0(t)$, is a key observable for interpreting earthquake source dynamics and the generation of ground motion (Vallée, 2013; Chu et al., 2009; Miyake, 2003; Hirano, 2022). It is defined as the time derivative of seismic moment M_0, and can be written as

$$\dot{M}_0(t) = \mu \iint_U \dot{u}(\mathbf{x}, t)\ \mathrm{d}A, \tag{1}$$

where μ is the shear modulus of the surrounding medium, $\dot{u}(\mathbf{x}, t)$ is the local slip rate, and U is the entire fault surface, representing the instantaneous rate of moment release as fault slip accumulates during earthquake rupture (e.g., Tocheport et al., 2007; Hirano, 2022). Its shape encodes the coupled evolution of rupture area growth and spatially averaged slip rate from initiation to arrest, revealing essential features including rupture

front propagation, slip rate variability, and rupture arrest mechanisms (Das & Kostrov, 1988; Tinti, 2005; Vallée, 2013). Consequently, constraining the physical mechanisms that govern the STF is central to advancing models of earthquake source physics and dynamic rupture, informing our understanding of radiated energy, stress drop, and seismic event scaling (Tocheport et al., 2007; Vallée, 2013; Vallée & Douet, 2016).

Classical seismic dynamic theories predict that, under uniform stress fields and symmetric rupture conditions, the STF exhibits specific temporal evolution patterns. Madariaga (1976) showed that this expansion produces quadratic moment rate growth $\dot{M}_0 \propto t^2$ during the initial rupture stage. However, STFs inferred from real earthquakes often deviate substantially from these symmetric predictions, and the physical origins of this variability remain incompletely understood. Denolle (2019) reported events whose early moment rate evolution agrees with the predicted t^2 scaling, whereas Meier et al. (2017) found many earthquakes exhibiting nearly linear growth, $\dot{M}_0 \propto t$, suggesting decoupling between rupture area expansion and average slip. A large-scale analysis by Renou et al. (2019) indicated a steeper average scaling of $\dot{M}_0 \propto t^{2.7}$, highlighting diversity beyond what any single theoretical model can fully explain. Together, these studies reveal that early STF growth exponents span from sub-quadratic ($\dot{M}_0 \propto t$) to super-quadratic ($\dot{M}_0 \propto t^{2.7}$), bracketing but not converging on the t^2 prediction of idealized self-similar expansion. Moreover, near-source observations that compare events on the same absolute timescale, rather than after normalization by duration or final moment, show that small and large earthquakes are statistically indistinguishable during their earliest growth (Meier et al., 2016; Noda & Ellsworth, 2016), with individual events departing from this common growth curve at a time that correlates with final magnitude (Noda & Ellsworth, 2016). These observations indicate that the early growth phase carries little information about the eventual rupture extent, suggesting that growth and arrest are governed by distinct physical controls. Such variability implies that STF evolution is governed by multiple interacting physical mechanisms, which may include rupture initiation location, background stress gradient, seismogenic zone geometry, and frictional weakening behavior, each capable of independently modifying the spatiotemporal evolution of slip rate and rupture area.

Several of these controls have been studied individually in the context of rupture dynamics, yet prior work has typically treated the STF as a secondary product of waveform inversion or benchmarked it against idealized self-similar models, rather than explicitly decomposing it into growth, steady, and arrest phases and mapping specific physical mechanisms to each segment. As a result, while the field has long observed that STF shapes vary, the physical levers responsible for distinct features of the moment rate curve, including growth-phase curvature, plateau duration, and arrest-phase decay, have not been systematically quantified. Dynamic rupture simulations by Ke et al. (2022) showed that rupture initiation at the center of an overstress zone (Reches & Fineberg, 2023) promotes radially symmetric rupture expansion consistent with classical t^2 scaling, whereas initiation near the edge produces predominantly unilateral rupture with approximately linear moment rate growth, prolonged growth phases, and delayed STF peaks—patterns consistent with observations of edge-nucleated earthquakes (Houston, 2001). Rupture geometry further modulates STF shape through confinement effects. In elongated seismogenic zones, rupture spread is constrained along the short axis, producing sustained quasi-steady moment release that manifests as a pronounced plateau before eventual decay (Weng & Ampuero, 2019). The arrest phase is likewise shaped by frictional behavior. Classical Linear Slip-Weakening (LSW) models (Ida, 1972; Palmer & Rice, 1973; Andrews, 1976b; Uenishi & Rice, 2003) predict abrupt termination, yet inversions of large earthquakes frequently yield long-tailed STFs that decay gradually (Duputel et al., 2013; Li, 2022), which a dual-scale weakening (Bažant, 2004; Paglialunga et al., 2022) can reproduce through gradual stress reduction governed by an extended secondary weakening that follows the initial weakening. The background stress gradient outside the overstress zone provides an additional, independent control on arrest: laboratory experiments

and dynamic rupture simulations show that the initial stress distribution, rather than the cohesive zone alone, governs the slip taper and stress transition at the rupture tip, defining what has been termed the earthquake arrest zone (Ke et al., 2021; Cebry, Ke, & McLaskey, 2022). Consequently, while each mechanism individually offers a partial explanation for observed STF variability, their relative contributions and combined effects on STF scaling across the growth, steady, and arrest phases remain unquantified.

Here we employ systematic numerical experiments to quantify how rupture initiation location (Ke et al., 2022), background stress gradient (Ke et al., 2022, 2021), seismogenic zone geometry (Weng & Ampuero, 2019), and frictional weakening (Paglialunga et al., 2022), each previously examined as an independent control on rupture dynamics, jointly govern STF evolution across the growth, steady, and arrest phases. We vary each parameter independently, and where applicable in combination, to isolate their separate contributions. By establishing quantitative relationships between rupture characteristics and observable STF features, including growth-phase scaling exponents, plateau duration, peak timing, and arrest-phase shape, this study provides a systematic basis for understanding how their interplay produces the diversity of STF shapes observed in natural earthquakes. Our results demonstrate that the wide variety of observed STF shapes can arise from multiple physical processes acting simultaneously, with rupture initiation location primarily governing early-phase symmetry and growth curvature, geometric confinement controlling plateau development and duration, and background stress gradient and frictional weakening jointly determining arrest-phase behavior. These findings provide an improved physical basis for seismic source inversion and enhance understanding of near-fault ground motion generation.

2 Methods

The numerical simulations are derived from Ke et al. (2022) using UGUCA (Kammer et al., 2021a), an open-source implementation of the spectral-boundary-integral method (Geubelle & Rice, 1995; Breitenfeld & Geubelle, 1998), to simulate spontaneous rupture propagation on a two-dimensional fault plane embedded in a three-dimensional homogeneous elastic medium under a non-uniform initial stress field. The medium is linear elastic with Young's modulus $E = 30$ GPa, Poisson's ratio $\nu = 0.25$ (shear modulus $\mu = 12$ GPa), and density $\rho = 2655$ kg/m^3. This framework efficiently simulates stress, slip, and rupture evolution and has been widely applied to investigate both laboratory earthquakes (e.g., Cebry, Ke, Shreedharan, et al., 2022; Okubo et al., 2026) and natural earthquakes (e.g., Lapusta et al., 2000; Lambert et al., 2021), making it well suited to examining the physical controls on the growth, steady, and arrest phases of the STF. By design, the simulation setup allows each candidate mechanism, namely rupture initiation location, overstress zone geometry, background stress gradient, and frictional weakening behavior, to be varied independently, and where applicable in combination, enabling systematic isolation of their individual contributions as well as characterization of their coupled effects on moment-release dynamics. This directly addresses the limitation that previous studies have typically examined these controls in isolation, which has obscured how their interactions shape moment-release dynamics across the growth, steady, and arrest phases of the STF. By enabling joint variation of these mechanisms, this approach provides a more comprehensive assessment of their coupled influences and allows for a clearer physical interpretation of how each control operates both independently and in combination with the others.

2.1 Initial stress distribution

The initial stress distribution follows Ke et al. (2022), whose key feature is an overstress zone surrounded by a continuous, radially decaying shear stress gradient (Fig. 1a) that enables rupture arrest while keeping fracture energy constant. For a circular over-

stress zone with radius $a = 1.2$ m, the initial shear stress τ_i is constant at $\tau_i(r) = \alpha$ when $r \leq a$ and decreases linearly with distance outside as $\tau_i(r) = \alpha - \beta(r - a)$ for $r > a$, where $\alpha = 67.5$ MPa is the uniform shear stress level within the overstress zone and $\beta = 18.75$ MPa/m is the stress decay rate in the surrounding region (Fig. 1a). A larger β corresponds to a steeper stress reduction outside the overstress zone, whereas a smaller β yields a more gradual gradient. The region where τ_i drops below the residual shear strength τ_r (defined in Section 2.2) constitutes the arrest zone, where the stress deficit progressively decelerates and ultimately stops the rupture front, controlling the conditions under which rupture terminates. The effect of β on STF arrest-phase shape is examined systematically in Section 3. This configuration maintains continuity and smoothness of the stress field, providing well-defined conditions for both rupture propagation and arrest.

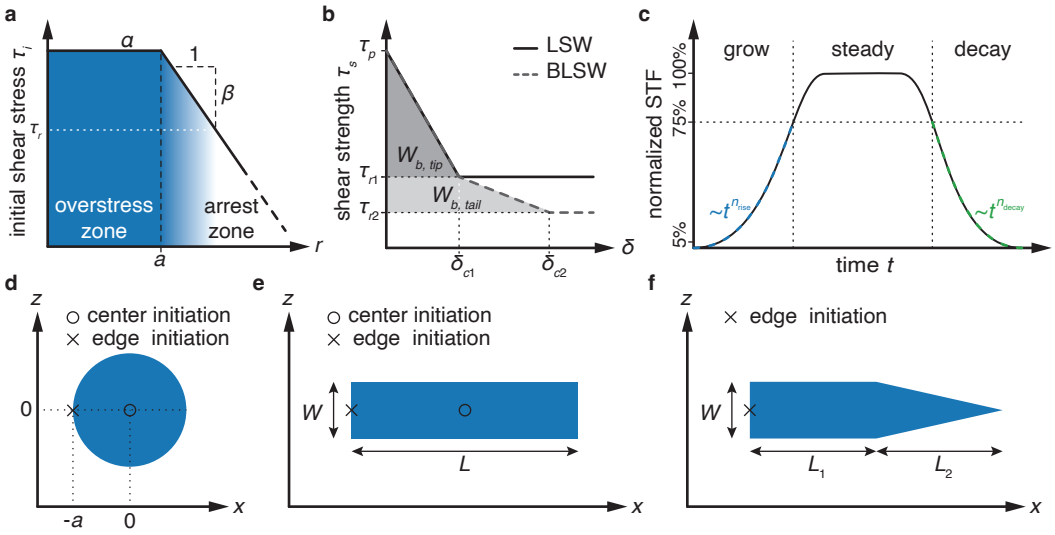


Figure 1: **Numerical model setup and geometric configurations.** (a) Prescribed initial shear-stress distribution: the stress is uniform at $\tau_i = \alpha$ inside the overstress zone ($r \leq a$) and decreases linearly with slope $\mathrm{d}\tau_i/\mathrm{d}r = -\beta$ for $r > a$. The arrest zone corresponds to the region where $\tau_i < \tau_r$, providing a stress deficit that arrests the rupture. (b) Shear strength evolution for the linear slip-weakening (LSW) and bilinear slip-weakening (BLSW) laws, highlighting the weakening distances δ_{c1} and δ_{c2} and residual strength levels τ_{r1} and τ_{r2}. (c) Schematic of a normalized STF illustrating the three-phase partition used in this study. The growth and arrest phases span the intervals below 75% of the peak amplitude on the rise and decay sides, respectively, and the steady phase is the intermediate interval above this threshold during which moment release remains approximately sustained. (d) Circular overstress patch (radius a) with center and edge initiation locations. (e) Rectangular overstress patch of width W and length L with center and edge initiation locations. (f) Tapered overstress patch characterized by width W, proximal length $L_1 = 5W$, and distal taper length L_2, with edge initiation at the wide end.

2.2 Friction laws

The fault shear strength is described by slip-weakening friction laws (Fig. 1b). To separately compare the effects of different weakening forms, we employ both the conventional linear slip-weakening (LSW) law (Ida, 1972; Palmer & Rice, 1973; Andrews, 1976b; Uenishi & Rice, 2003) and a bilinear slip-weakening (BLSW) law (Paglialunga et al., 2022) with an extended weakening tail that approximates the dual-scale weakening behavior

(Bažant, 2004). For the LSW law, we adopt the same parameters as Ke et al. (2022): peak shear strength $\tau_p = 80$ MPa, residual shear strength $\tau_r = 60$ MPa, and slip-weakening distance $\delta_c = 10$ µm. In the suite of simulations dedicated to frictional weakening, we fix the rupture initiation location at the center to maintain geometric symmetry and use it as a reference condition for comparing different weakening forms. To extend this baseline into a two-stage weakening framework, the frictional behavior follows the BLSW law, which retains the first-stage parameters of the LSW law ($\tau_p = 80$ MPa, $\delta_{c1} = 10$ µm, and $\tau_{r1} = 60$ MPa) and appends a secondary weakening tail terminating at a final residual shear stress $\tau_{r2} = 55$ MPa. We systematically change only the secondary weakening distance δ_{c2}, with a reference value of 12.5 µm, while holding the primary weakening parameters fixed. The primary weakening stage governs the nucleation process and growth-phase dynamics, so fixing δ_{c1}, τ_p, and τ_{r1} ensures that the early growth phase remains identical across all BLSW cases and that any differences in rupture propagation and seismic moment release can be attributed unambiguously to the extent of the tail-weakening segment. Because τ_p, τ_{r1}, τ_{r2}, and δ_{c1} are held fixed, specifying δ_{c2} uniquely determines the secondary weakening rate w_2, while the total strength drop, and hence the static stress-drop budget, is identical across the suite. Varying δ_{c2} alone therefore isolates the effect of the secondary weakening length scale at fixed strength drop, and, as shown in Section 3.4, this single parameter modifies both the growth and the arrest phases of the STF, from LSW-like abrupt termination to smoother, long-tailed arrest behavior.

2.3 Rupture geometry and initiation

To investigate the effect of rupture geometry on the STF, we consider three overstress-zone shapes, circular, rectangular, and pentagonal (Fig. 1d,e,f), while holding the friction parameters fixed under the LSW law for all geometry cases. This design is motivated by prior dynamic rupture studies showing that STF evolution can be sensitive to rupture initiation conditions and fault geometry (Ke et al., 2022; Weng & Ampuero, 2019; Houston, 2001).

In all simulations, rupture is nucleated by a circular seed crack that grows from zero radius at the prescribed rupture initiation location. Within the seed crack, the peak strength τ_p is manually reduced to the residual strength τ_r, effectively eliminating fracture energy, while the crack front expands at 10% of the Rayleigh wave speed. Once the size of the seed crack reaches the Griffith length (Andrews, 1976a), the rupture front spontaneously accelerates to the Rayleigh wave speed and subsequently remains nearly stable throughout propagation. Rupture is initiated with a slowly extending seed crack, following standard practice in spectral boundary-integral simulations of spontaneous fault rupture (Kammer et al., 2021a; Ke et al., 2021, 2022). The prescribed expansion speed does not influence the resulting STF. Varying it between 1% and 50% of the Rayleigh wave speed shifts only the onset time of spontaneous rupture, and the STF shapes for both center and edge initiation are indistinguishable once aligned on their peaks (Figs. S4 and S5). In this way, rupture evolution is governed by the prescribed stress field and friction law, enabling direct comparison of geometry, initiation location, and frictional weakening.

For the circular overstress zone, we consider five different rupture initiation locations: the center and locations at radial distances $0.25a$, $0.50a$, $0.75a$, and $1.00a$ from the center, representing a transition from centered to increasingly off-centered initiation (Fig. 1d). This design allows us to quantify how changes in rupture initiation location affect the expansion of rupture area and, in turn, the STF growth laws (particularly t vs. t^2 growth).

For the rectangular overstress zone (Fig. 1e), we prescribe six aspect ratios (L/W) of 1, 5, 10, 15, 20, and 30, extending the elongated fault geometry framework of Weng

and Ampuero (2019) to systematically examine how increasing geometric confinement along the short axis generates plateau-like steady phases in the STF. All rectangular zones share a fixed short-axis width $W = 0.24$ m, so the square case is an order of magnitude smaller in linear dimension than the circular reference of radius $a = 1.2$ m. Comparisons between the circular and rectangular families therefore reflect a difference in characteristic dimension as well as in shape; the control suite of Fig. S11, in which the rectangular configurations are enlarged tenfold, separates the two effects. The small fixed width is a computational choice rather than a physical one, adopted to make this wide range of aspect ratios computationally affordable. These aspect ratios span from a square patch to a highly elongated strip-like overstress region, imposing different degrees of geometric constraint on rupture growth along the short axis. Each rectangular case includes two rupture initiation locations, center initiation and edge initiation. Center initiation tends to produce relatively symmetric rupture, whereas edge initiation enhances directivity and facilitates quasi-steady slip along the long axis.

Building on this, we additionally design a series of pentagonal overstress zones (Fig. 1f) with four values of L_2/W equal to 0, 2, 4, and 6, all with edge initiation and $L_1 = 5W$, focusing on how rupture entering a geometrically tapered region modifies the arrest phase. The motivation for this geometry is the arrest behavior that the preceding configurations cannot produce. In circular and rectangular overstress zones the moment-releasing area is extinguished abruptly once the rupture front reaches the far boundary (Ke et al., 2018), whereas the STFs of natural earthquakes commonly decay far more gradually (Vallée & Douet, 2016). For a gradual arrest to arise from geometry alone, the available rupture area must diminish progressively as the front advances, and a linearly narrowing width is the simplest realization of this requirement. The pentagon is thus an illustrative, exploratory idealization rather than a representation of any specific natural fault geometry. It nevertheless has a natural counterpart. The down-dip extent of coseismic slip is bounded by creeping, velocity-strengthening regions (Scholz, 1998; Jiang & Lapusta, 2016), and the depth of this locked-to-creeping transition varies along strike (Smith-Konter et al., 2011), so that a rupture propagating along strike can encounter a progressively narrowing rupturable width, for example on approach to a creeping fault section. Fault steps and segment boundaries, where ruptures preferentially terminate (Wesnousky, 2006), instead produce the abrupt arrest represented by the $L_2/W = 0$ end-member. The proximal length $L_1 = 5W$ is chosen to ensure that the rupture reaches a quasi-steady propagation regime before encountering the tapered distal region, consistent with the width-saturated regime identified by Weng and Ampuero (2019) in which the energy release rate becomes length-independent, so that differences in the arrest phase can be attributed unambiguously to the taper geometry rather than to transient growth-phase dynamics. Edge initiation is prescribed because unilateral propagation toward the taper produces a well-defined, directionally coherent arrest that is most sensitive to L_2/W, whereas bilateral initiation would superpose two competing arrest fronts and obscure the taper effect, a conclusion directly supported by the rectangular simulations which show that edge initiation consistently generates a more pronounced and interpretable plateau than center initiation for the same aspect ratio. The range $L_2/W = 0$ to 6 is selected so that the $L_2/W = 0$ case serves as a rectangular baseline ($L/W = 5$) against which the progressive effect of increasing taper length can be assessed, spanning the transition from a nearly abrupt arrest to a substantially prolonged and gradual decay in which the converging geometry dominates the termination process.

2.4 STF analysis

For each simulation, we compute the complete moment-rate time history $\dot{M}_0(t)$, i.e., the STF, and characterize its shape using a set of quantitative metrics defined below. We define t_{begin} and t_{end} as the first and last instants when $\dot{M}_0(t)$ exceeds 5% of its peak value, the STF duration as $T = t_{\text{end}} - t_{\text{begin}}$, and the normalized peak time as $\hat{t}_{\text{peak}} = (t_{\text{peak}} - t_{\text{begin}})/T$. The 5% threshold matches the thresholded duration def-

initions used for observational STFs (Vallée & Douet, 2016), and it keeps T and $\hat{t}_{\mathrm{peak}}$ well defined for long-tailed decays whose moment rate vanishes only asymptotically. The fitted exponents do not involve this threshold: the windows of the power-law fits introduced below are delimited by the 75% crossings rather than by the onset threshold, and the time shifts t_i and t_f are free fit parameters.

Each STF is conceptually partitioned into three physically motivated phases consistent with the general rupture development inferred from dynamic rupture modeling and STF observations (Weng & Ampuero, 2019; Meier et al., 2017; Renou et al., 2019; Houston, 2001): a growth phase during which the STF rises rapidly, a steady phase during which the STF remains approximately sustained, and an arrest phase during which the STF decreases to zero. To operationally delineate these phases, we use 75% of the peak amplitude $\dot{M}_0^{\mathrm{peak}}$ as the threshold (Fig. 1c), a level chosen to exclude the strongly curved portions near the peak while retaining a sufficient interval on both the rise and decay sides to constrain the power-law fits reliably.

To quantify the curvature of the growth and arrest phases, we fit power-law functions separately to each segment. For the growth phase, the STF is fitted using

$$\dot{M}_0(t) = a_{\mathrm{rise}}\,(t - t_i)^{n_{\mathrm{rise}}}, \tag{2}$$

where a_{rise}, t_i, and n_{rise} are the scaling constant, time-shift, and curvature exponent, respectively, all treated as free parameters in the fit. Larger values of n_{rise} indicate a more strongly curved and rapidly accelerating rise, with the classical self-similar prediction corresponding to $n_{\mathrm{rise}} = 2$ (Madariaga, 1976). For the arrest phase, the STF is fitted using

$$\dot{M}_0(t) = a_{\mathrm{decay}}\,(t_f - t)^{n_{\mathrm{decay}}}, \tag{3}$$

where a_{decay}, t_f, and n_{decay} are the scaling constant, time-shift, and curvature exponent, respectively, all treated as free parameters in the fit. Larger values of n_{decay} correspond to a steeper and more abrupt termination, whereas smaller values indicate a smoother and more prolonged decay. All fitting parameters are estimated using nonlinear least-squares inversion, and the coefficient of determination R^2 is used to assess fitting quality. The fitted exponents are descriptive shape metrics over these defined windows, and we interpret them physically only where the fitted phase is genuinely power-law-like. Across all tabulated cases the fits are excellent, with $R^2 \geq 0.994$. The simulation setup parameters and all fitted metrics for each simulation suite are provided in Tables S1–S12 of the Supporting Information. Figure S8 additionally presents the STFs of every suite in duration- and moment-normalized form relative to each suite's reference case.

These metrics provide a direct link to observational constraints on STF shape reported in the literature. For n_{rise}, published estimates span from approximately 1, corresponding to the nearly linear growth reported by Meier et al. (2017) for many earthquakes, to 2, consistent with the classical self-similar t^2 prediction (Madariaga, 1976; Denolle, 2019), to values exceeding 2, with Renou et al. (2019) reporting a steeper average scaling of $\dot{M}_0 \propto t^{2.7}$ from a large-scale analysis. For $\hat{t}_{\mathrm{peak}}$, a value near 0.5 indicates a nearly symmetric STF consistent with the classical bilateral rupture picture, whereas values substantially below 0.5 indicate an early-peaking STF with a prolonged decay tail, a pattern that is in fact common in cataloged natural earthquakes (Vallée & Douet, 2016). Values substantially above 0.5 reflect a strongly asymmetric STF, with a ramp-like rise followed by a more abrupt decay, a pattern commonly associated with unilateral rupture and rupture directivity (Houston, 2001; Vallée & Douet, 2016). Together, these observational benchmarks define the target range against which the simulation results are compared in the following sections.

3 Results

3.1 Effect of rupture initiation location

To isolate the role of rupture initiation location, we compare five discrete initiation points spanning from the center to the edge of a circular overstress zone (at radial distances 0, $0.25a$, $0.50a$, $0.75a$, and $1.00a$ from the center) while keeping overstress zone geometry, background stress gradient β, and friction fixed (Fig. 2). In the reference simulation where rupture initiates at the center, the growth and decay phases are close to parabolic ($n_{\mathrm{rise}} = 2.04$ and $n_{\mathrm{decay}} = 2.46$), and the peak occurs at $\hat{t}_{\mathrm{peak}} = 0.52$, close to the midpoint of the STF duration, reflecting a nearly symmetric shape. The velocity snapshots confirm that center initiation produces a radially symmetric expanding rupture front (Fig. 2a), whereas edge initiation produces a strongly asymmetric, predominantly unilateral expansion in which the rupture front propagates preferentially away from the initiation point (Fig. 2b). As the rupture initiation location is progressively shifted toward the edge, the STF shape becomes increasingly asymmetric, with both the rise and decay durations increasing while the rise duration increases more substantially, shifting $\hat{t}_{\mathrm{peak}}$ from 0.52 to 0.62 and reducing the peak moment rate (Fig. 2c). The reduction in peak moment rate with increasing offset reflects the transition from bilateral to unilateral rupture expansion, as a progressively larger fraction of the potential rupture area lies in the direction away from the boundary, limiting the total rate of area growth and thus the peak moment release rate. This transition is also captured quantitatively by the fitted exponents: n_{rise} decreases from 2.04 at center initiation to $\sim$1 at the edge, indicating a shift from quadratic to nearly linear growth as the rupture transitions from bilateral to unilateral expansion (Meier et al., 2017), while n_{decay} is lower for off-center initiation, between 1.60 and 1.88 compared with 2.46 at the center, reflecting a smoother arrest phase. The cumulative slip profiles show that during propagation the two cases evolve differently, with edge initiation producing a more asymmetric transient slip distribution, while the final slip profiles are nearly identical between the two cases (Fig. 2d,e).

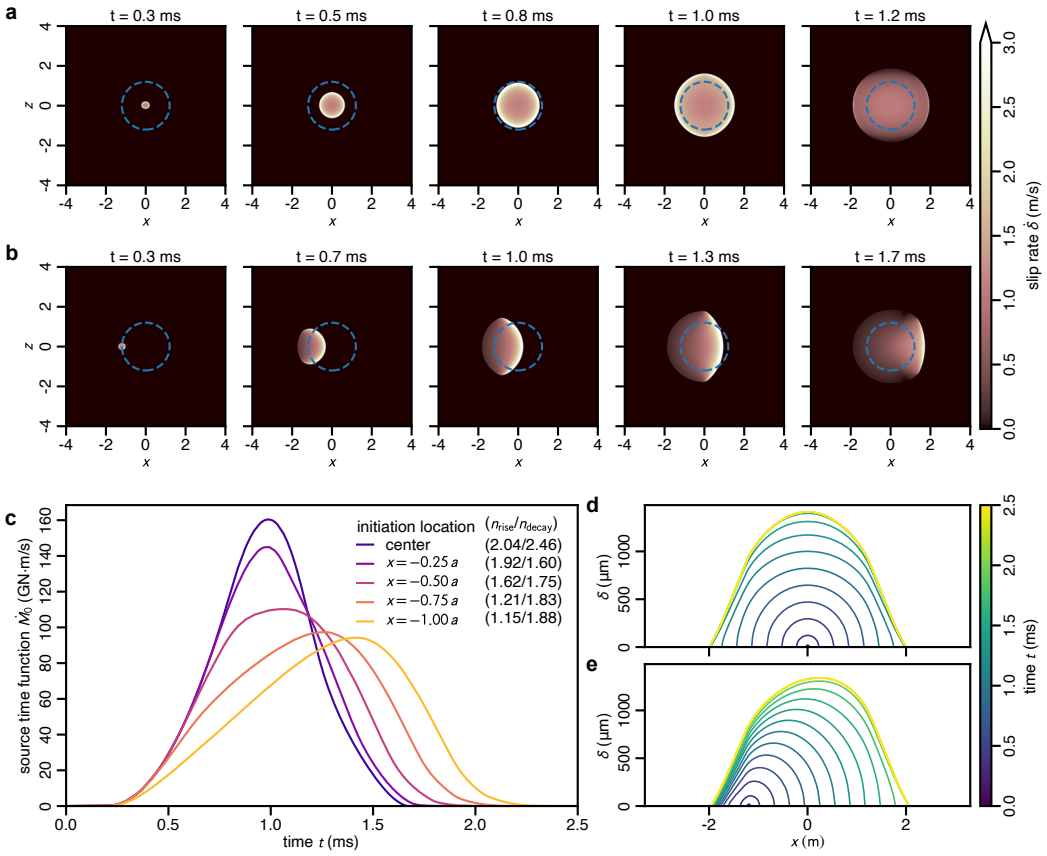


Figure 2: **Effect of rupture initiation location in a circular overstress zone.** (a, b) Snapshots of slip velocity on the fault plane for rupture initiated at the (a) center and (b) edge of the circular overstress zone. The blue dashed circle marks the boundary of the high-stress plateau where $\tau_i = \alpha$. (c) Source time functions for five initiation locations ranging from the center to the edge of the overstress zone, as indicated in the legend. (d, e) Cumulative slip profiles along the x-axis at z=0 as a function of time for the (d) center and (e) edge initiation cases, with line color indicating elapsed time.

3.2 Effect of background stress gradient

To isolate the effect of the background stress gradient on STF shape, we conduct simulations across five values of β spanning 18.75 to 300 MPa/m, while keeping rupture initiation location at the center, overstress zone geometry circular, and friction law fixed. Because the initial stress within the overstress zone is identical across all five cases by construction, the growth phases of the STFs are also identical (Fig. 3c), with the fitted exponent $n_{\text{rise}} \approx 2.05$ remaining virtually unchanged across all β values, confirming that β has no effect on early rupture expansion since the rupture front does not encounter the stress gradient until after it exits the high-stress plateau ($\tau_i = \alpha$). By contrast, β exerts systematic and pronounced control on both the arrest-phase duration and curvature once the rupture front exits the high-stress plateau (Fig. 3c). Decreasing β produces a shallower stress gradient, which sustains the rupture front for a longer distance after it exits the overstress zone, resulting in a higher peak moment rate, a longer total STF duration, and a smoother, more gradual decay with smaller n_{decay}. Increasing β steepens the gradient, depleting the driving stress ahead of the rupture front more rapidly and producing a shorter, more abrupt termination with larger n_{decay}. Quantitatively,

n_{decay} increases from 2.46 at $\beta = 18.75$ MPa/m to 4.12 at $\beta = 300$ MPa/m, while the STF duration T decreases from 1.21 to 0.87 ms over the same range. The normalized peak time $\hat{t}_{\text{peak}}$ shifts modestly from 0.52 to 0.55 with increasing β, reflecting the disproportionate shortening of the arrest phase relative to the growth phase. The velocity snapshots confirm this contrast, with small β allowing the rupture front to propagate well beyond the overstress zone boundary before decelerating and to approach the contour where τ_i drops to zero, whereas large β causes the rupture front to decelerate sharply near the overstress zone boundary (Fig. 3a,b). The cumulative slip profiles are consistent with this interpretation, as small β produces a broadly tapered slip distribution that extends well beyond the overstress zone boundary (Fig. 3e), whereas large β confines the final slip more sharply with steeper tapers at the rupture tips (Fig. 3d). Taken together, the five β cases show that arrest-phase duration and curvature scale monotonically with β, while the growth phase remains unaffected, establishing β as an independent and quantifiable control on STF shape for centered initiation. In a companion suite combining edge initiation with the same five β values (Fig. S6 and Table S11), part of the rupture front propagates into the gradient from the outset, and the growth exponent acquires a mild dependence on β, with n_{rise} increasing and saturating, while remaining far below the centered value. The monotonic arrest-phase control of β persists at edge initiation, though the range of n_{decay} widens, so the two controls remain qualitatively separable even when acting together.

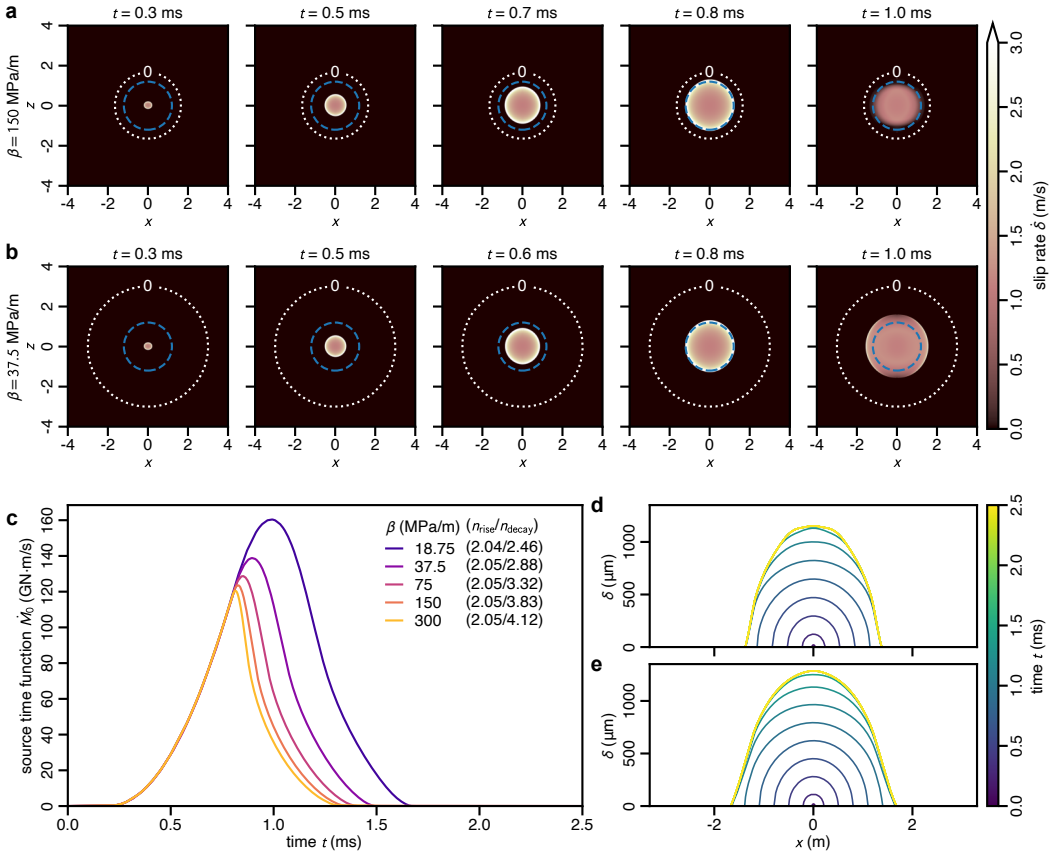


Figure 3: **Effect of the background stress gradient β on dynamic rupture propagation.** (a, b) Snapshots of slip velocity on the fault plane for (a) $\beta = 150$ MPa/m and (b) $\beta = 37.5$ MPa/m. The blue dashed circle marks the boundary of the high-stress plateau ($\tau_i = \alpha$), and the white dotted circle marks the contour where τ_i drops to zero. (c) Source time functions for five values of β ranging from 18.75 to 300 MPa/m, as labeled in the legend. (d, e) Cumulative slip profiles along the x-axis at $z = 0$ for (d) $\beta = 150$ MPa/m and (e) $\beta = 37.5$ MPa/m; line color indicates elapsed time.

3.3 Effect of overstress zone geometry

To investigate the control of overstress zone geometry on the STF, we consider three overstress zone shapes (circular, rectangular, and pentagonal; Fig. 1d,e,f) using identical friction parameters under the LSW law in all geometry cases. By holding friction fixed and changing only geometry and rupture initiation location, this design isolates their individual contributions to STF shape, directly addressing the gap left by prior studies that treated these controls separately (Ke et al., 2022; Weng & Ampuero, 2019; Houston, 2001). To examine how overstress zone geometry shapes the STF, we prescribe aspect ratios of rectangular overstress zones across a wide range ($L/W = 1$ to 30) and the second principal length scale of pentagonal zones ($L_2/W = 0$ to 6), with rupture initiation location included as a secondary parameter in the rectangular case to illustrate its interaction with confinement. Overstress zone geometry modulates STF shape through confinement effects, and rupture initiation location continues to play a secondary role within geometrically constrained zones.

For the rectangular overstress zone, the STF shape depends jointly on aspect ratio and initiation location (Fig. 4c). At low aspect ratio ($L/W = 1$, square), neither central nor edge initiation produces a plateau, and the STF resembles the circular case, with $\hat{t}_{\mathrm{peak}} \approx 0.52$ for both initiation locations. However, $n_{\mathrm{rise}} \approx 1.4$ is already noticeably lower than the value of 2.04 observed for center initiation in the circular overstress zone. This difference reflects boundary-contact timing rather than the shape itself. Because the square's half-width is only 0.12 m, the rupture front crosses the overstress boundary while the moment rate is still below 1% of its eventual peak, so essentially all of the moment release in the fitted rise occurs after boundary contact, and the fitted exponent measures propagation into the surrounding stress gradient rather than growth inside the overstressed region. In the circular reference, by contrast, the front reaches the patch boundary within a few percent of the peak time, and the fitted rise measures the self-similar expansion phase. As the aspect ratio increases, central initiation leads to a predominantly bilateral rupture with a developing plateau, reflecting the increasing dominance of long-axis rupture propagation. The apparent decrease in n_{rise} with increasing L/W for center initiation, from 1.37 at $L/W = 1$ to 0.90 at $L/W = 20$, is attributable to the development of the plateau rather than a change in the underlying growth dynamics. As shown in Fig. 4c, the growth phases of all center initiation cases overlap, confirming that the growth dynamics are unaffected by aspect ratio, and as the plateau becomes more pronounced the 75% threshold used to delineate the growth phase captures a progressively smaller and shallower portion of the rise, resulting in a lower fitted exponent. Edge initiation consistently reduces the peak moment rate to approximately one-half of the central initiation value for the same aspect ratio, promotes unilateral propagation, and produces a clear quasi-steady plateau in which $\dot{M}_0(t)$ remains elevated for an extended period before the final decay (Fig. 4a,b). The plateau duration increases systematically with aspect ratio for both initiation locations, as evidenced by the progressive increase in T_{steady} from 0.17 ms at $L/W = 1$ to 3.7 ms at $L/W = 30$ for edge initiation. The slip profiles confirm that edge initiation produces pulse-like slip histories along the fault, in which slip is locally confined to a traveling window rather than accumulating continuously behind the rupture front (Fig. 4d,e), consistent with the self-healing slip-pulse interpretation of Heaton-type rupture behavior (Heaton, 1990; McLaskey et al., 2015). Notably, this pulse-like behavior emerges spontaneously from the geometric confinement of the rectangular overstress zone rather than from any explicit self-healing mechanism in the friction law, distinguishing it from earlier models in which self-healing was attributed to frictional restrengthening or aging/contact-healing in stationary contact (Perrin et al., 1995; Zheng & Rice, 1998; Pomyalov et al., 2023).

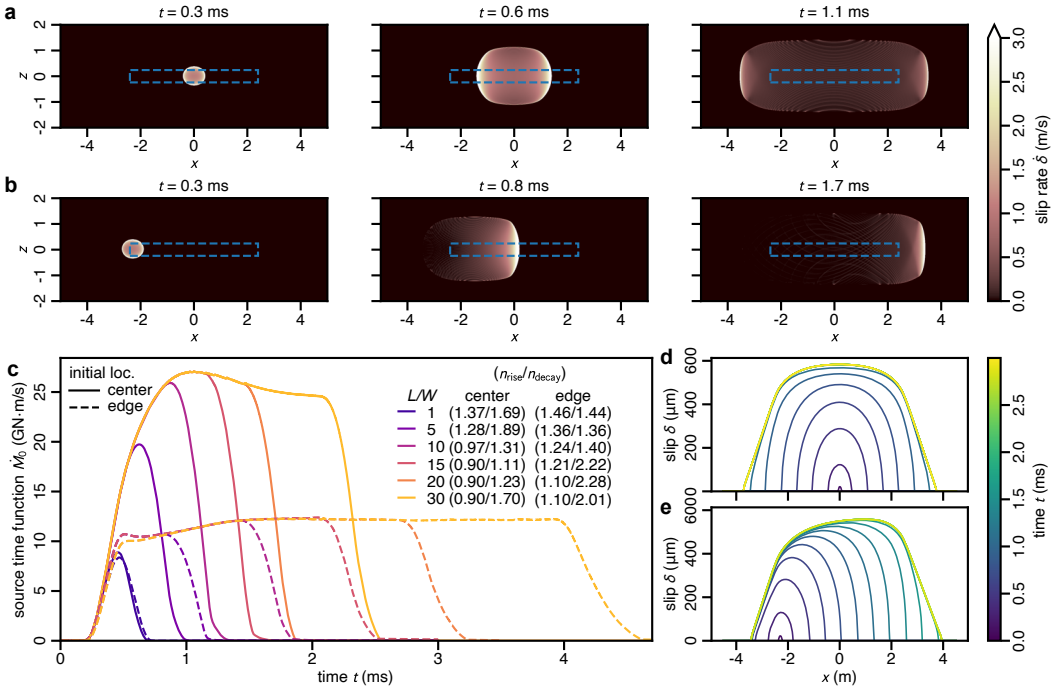


Figure 4: **Effect of rupture initiation location and aspect ratio in a rectangular overstress zone.** (a, b) Snapshots of slip velocity on the fault plane for rupture in a L/W=10 rectangular overstress zone initiated at the (a) center and (b) edge. The blue dashed rectangle marks the boundary of the high-stress plateau where $\tau_i = \alpha$. (c) Source time functions for rectangular overstress zones with aspect ratios ranging from L/W=1 to 30 and both center (solid) and edge (dashed) initiation locations, as indicated in the legend. (d, e) Cumulative slip profiles along the x-axis at z=0 as a function of time for the L/W=10 case with (d) center and (e) edge initiation, with line color indicating elapsed time.

For simulations with a pentagonal overstress zone, the $L_2/W = 0$ case reduces exactly to the rectangular $L/W = 5$ edge initiation case and serves as the baseline, with $n_{\text{decay}} = 1.36$ and $T_{\text{decay}} = 0.16$ ms consistent with the rectangular results. The growth phases of the STFs are identical across all four values of L_2/W (Fig. 5c), as expected from the identical proximal geometry ($L_1 = 5W$) shared by all cases. By contrast, the arrest phase is systematically controlled by L_2/W (see the geometric definition in Section 2). As L_2/W increases from 0 to 6 and the geometry becomes more elongated, the arrest phase becomes progressively longer and more gradual, consistent with the rupture front encountering a more extended tapering of the overstress region before finally arresting. Quantitatively, n_{decay} decreases from 1.36 at $L_2/W = 0$ to 0.81 at $L_2/W = 6$, while T_{decay} increases from 0.16 ms to 0.40 ms over the same range. In contrast, n_{rise} remains nearly constant at 1.34 to 1.36 across all cases and T_{rise} is likewise unaffected by L_2/W, confirming that the taper geometry acts exclusively on the arrest phase, while T_{steady} increases with L_2/W as a consequence of the more gradual decay keeping the STF above the 75% threshold for a longer interval. The velocity snapshots confirm that for larger L_2/W the rupture front remains active well into the tapered region before decelerating (Fig. 5a,b). The cumulative slip profiles show that larger L_2/W produces a more gradual arrest, with the slip front on the arrest side continuing to advance over a longer time interval before the rupture finally stops (Fig. 5d,e). The final slip amplitude is nearly identical between the two cases, which is expected for the pulse-like rupture behavior established in the rectangular cases (Fig. 4d,e), since the total slip accumulated at any point

is governed by the duration of the passing slip pulse rather than by the arrest geometry.

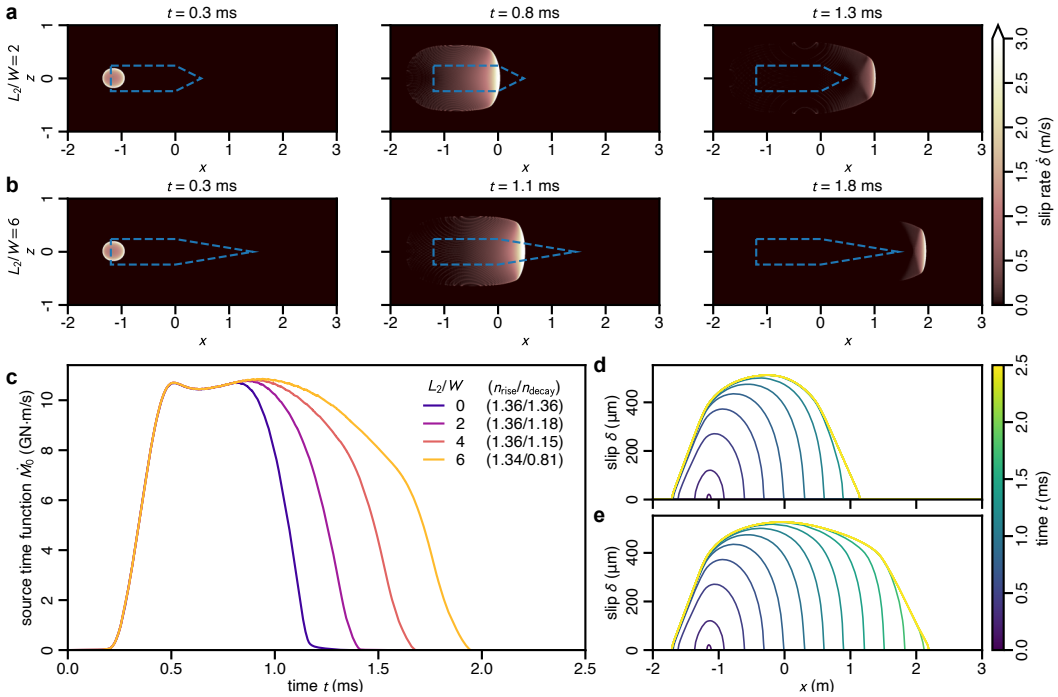


Figure 5: **Effect of the second characteristic length L_2 on rupture in pentagonal overstress zones.** (a, b) Snapshots of slip velocity on the fault plane for a pentagonal overstress zone with (a) L_2/W=2 and (b) L_2/W=6. The blue dashed outline marks the boundary of the high-stress plateau where $\tau_i = \alpha$. (c) Source time functions for pentagonal overstress zones with L_2/W ranging from 0 to 6, as indicated in the legend. Note that the growth phase is nearly identical across all cases, while the arrest phase lengthens systematically with increasing L_2/W. (d, e) Cumulative slip profiles along the x-axis at $z = 0$ as a function of time for (d) L_2/W=2 and (e) L_2/W=6, with line color indicating elapsed time.

3.4 Effect of frictional weakening

To isolate the effect of frictional weakening on STF shape, we conduct simulations across six values of the secondary weakening distance δ_{c2} ranging from 12.5 to 2000 µm in the bilinear slip-weakening friction law (BLSW, Fig. 1b) while keeping the background stress gradient, rupture initiation location, overstress zone geometry, and all primary weakening parameters fixed. The smallest value, δ_{c2} = 12.5 µm, is chosen so that the secondary weakening slope extrapolates the initial weakening slope beyond δ_{c1}, effectively approximating LSW behavior and serving as the reference case closest to linear slip-weakening (LSW). The upper bound of δ_{c2} = 2000 µm is selected because at this value the final slip over most of the high-stress plateau region ($\tau_i = \alpha$) exceeds δ_{c2} itself (Fig. 6d,e), meaning that the secondary weakening phase is fully developed across the majority of the overstress zone and further increasing δ_{c2} would produce diminishing additional effect on the STF shape. Although the primary weakening stage is identical across all cases, the growth phases of the STFs are not entirely decoupled from δ_{c2}, as the curves overlap during the very early rise but progressively diverge as more fault area enters the secondary weakening regime, indicating that the secondary weakening tail begins to influence moment

release before the peak is reached. For sufficiently large secondary weakening distances ($\delta_{c2} \geq 1000$ µm), this effect is strong enough to produce super-quadratic growth, with n_{rise} rising from 1.93 at $\delta_{c2} = 500$ µm to a maximum of 2.47 at $\delta_{c2} = 1000$ µm before decreasing gradually to 2.23 at $\delta_{c2} = 2000$ µm (Table S10), indicating that the secondary weakening tail actively accelerates moment release during the growth phase rather than merely modifying the arrest phase.

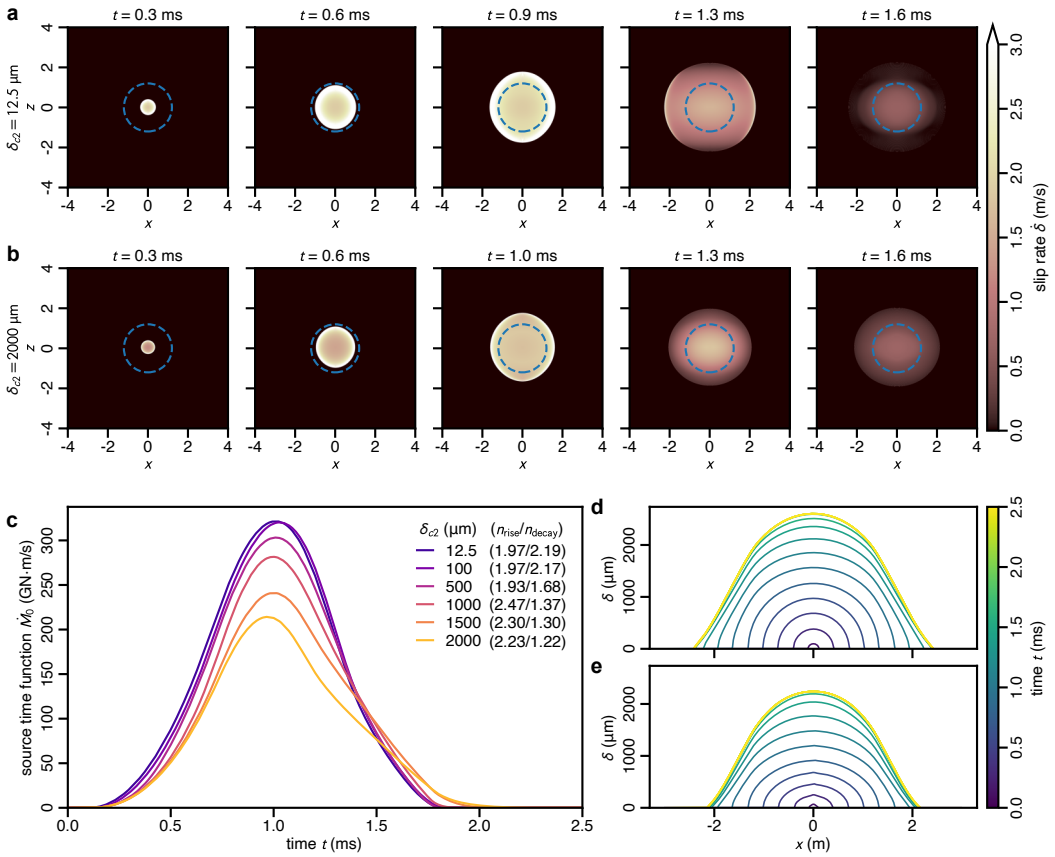


Figure 6: **Effect of the secondary slip-weakening distance δ_{c2} on dynamic rupture and STF shape.** (a, b) Snapshots of slip velocity on the fault plane for (a) $\delta_{c2} = 12.5$ µm and (b) $\delta_{c2} = 2000$ µm. The blue dashed circle marks the boundary of the high-stress plateau ($\tau_i = \alpha$). (c) Source time functions for six values of δ_{c2} ranging from 12.5 to 2000 µm, as labeled in the legend. (d, e) Cumulative slip profiles along the x-axis at $z = 0$ for (d) $\delta_{c2} = 12.5$ µm and (e) $\delta_{c2} = 2000$ µm; line color indicates elapsed time.

As δ_{c2} increases, the STF shape changes systematically in three respects (Fig. 6c). First, the peak moment rate decreases substantially, from ∼320 GN m/s at $\delta_{c2} = 12.5$ µm to ∼210 GN m/s at $\delta_{c2} = 2000$ µm, reflecting the additional energy dissipated during the prolonged secondary weakening phase. Second, the arrest phase becomes progressively smoother and more prolonged, with n_{decay} decreasing from 2.2 toward 1.2 over the same range, reflecting the transition from abrupt LSW-like termination to a long-tailed decay. Third, the normalized peak time $\hat{t}_{\text{peak}}$ shifts progressively earlier with increasing δ_{c2}, from 0.52 at $\delta_{c2} = 12.5$ µm to 0.43 at $\delta_{c2} = 2000$ µm, as the lengthening arrest phase shifts the peak toward the beginning of the total STF duration. This shift toward $\hat{t}_{\text{peak}} <$

0.5 is consistent with the early-peaking, long-tailed STF shapes commonly documented in natural earthquake catalogs (Vallée & Douet, 2016).

The velocity snapshots confirm that for large δ_{c2} the slip velocity decays more gradually and remains more spatially uniform within the overstress zone, whereas for small δ_{c2} the slip velocity drops off more sharply following rupture arrest (Fig. 6a,b). The cumulative slip profiles reveal that smaller δ_{c2} produces higher peak final slip, reaching approximately 2600 µm at $\delta_{c2} = 12.5$ µm compared to approximately 2250 µm at $\delta_{c2} = 2000$ µm (Fig. 6d,e), consistent with the higher peak moment rate and larger total seismic moment observed for smaller δ_{c2}. The reduction in final slip with increasing δ_{c2} reflects the progressive redistribution of energy into the extended secondary weakening tail rather than into fault slip, so that a larger fraction of the fracture energy is consumed by the prolonged weakening process rather than driving additional slip accumulation. Figure S9 illustrates this balance on the stress-versus-slip diagram. Taken together, these results demonstrate that δ_{c2} governs STF asymmetry, arrest-phase curvature, peak moment rate, and total slip independently of the geometric and stress-gradient controls documented in the preceding subsections, providing a frictional mechanism capable of producing early-peaking, long-tailed STF shapes.

4 Discussion

The results presented above demonstrate that the four physical mechanisms examined here, namely rupture initiation location, background stress gradient β, overstress zone geometry, and the secondary slip-weakening distance δ_{c2} in the BLSW friction law, each govern a distinct and largely separable feature of the STF across its three phases. For the purposes of this discussion, we distinguish between macro-scale structural controls, by which we mean rupture initiation location and overstress zone geometry, and constitutive frictional controls, referring to δ_{c2}, noting that β occupies an intermediate role as a property of the stress field rather than the fault itself. We discuss the physical interpretation of these controls in turn, before addressing their coupled effects and implications for interpreting natural earthquake STFs.

4.1 Rupture initiation location and growth-phase curvature

In the baseline case of center initiation within a circular overstress zone, the STF exhibits a nearly parabolic rise consistent with the classical self-similar bilateral rupture picture (Madariaga, 1976). If the rupture front expands at an approximately constant speed, the slipping area grows as $A(t) \sim t^2$ while the spatially averaged slip rate $\overline{V}(t)$ remains roughly constant, giving $\dot{M}_0(t) \propto A(t)\,\overline{V}(t) \sim t^2$ and naturally producing a parabolic STF envelope with $n_{\mathrm{rise}} \approx 2$. The radial symmetry of both the rupture expansion and the surrounding arrest zone further ensures that the growth and arrest phases are approximately mirror images of each other, placing the peak near the midpoint of the STF duration and yielding $\hat{t}_{\mathrm{peak}} \approx 0.5$. As the initiation location is shifted toward the edge of the high-stress plateau, the rupture becomes increasingly unilateral and the overstress zone boundary restricts expansion in one direction, reducing the area-growth rate. As a result, n_{rise} decreases from 2.04 at center initiation to approximately 1 at edge initiation, consistent with the nearly linear STF growth reported in observational studies (Meier et al., 2017; Houston, 2001). Even under identical stress and friction conditions, the rupture initiation location therefore controls the spatiotemporal balance between area growth and slip-rate evolution, modifying both growth-phase curvature and peak timing. The separation of growth and arrest controls offers a dynamic-rupture rationale for the same-timescale observations of Meier et al. (2016) and Noda and Ellsworth (2016). In our simulations the growth phase is set by the initiation location and the friction law (Figs. 2 and 6), whereas arrest is governed by the background stress gradient and the overstress zone geometry (Figs. 3–5), parameters the expanding rupture front

has not yet encountered during early growth. Early moment rate evolution therefore carries little imprint of the eventual arrest conditions, consistent with the observation that final earthquake size cannot be forecast from rupture onsets (Meier et al., 2016). Site-specific hierarchical patch structure offers a complementary rationale for these same-timescale observations, with co-located small and large events sharing common onsets because they initiate on the same structures (Ide & Aochi, 2005; Ide, 2019), as discussed in Section 4.4. Our center-initiation cases, with $n_{\text{rise}} \approx 2$, reproduce the common near-quadratic early growth documented by these same-timescale studies. The coexistence of near-quadratic and nearly linear growth in observations is consistent with variability in initiation location. We note that our simulations vary conditions at a single nominal source size, so these cross-magnitude scaling observations constrain the interpretation of our growth phase rather than being directly testable within our suite.

4.2 Background stress gradient and arrest-phase duration

The background stress gradient β controls the spatial extent of the arrest zone and thereby governs arrest-phase duration and curvature independently of geometry and friction. Because the initial stress within the overstress zone is identical across all β cases by construction, the growth phases of the STFs are also identical, and β acts exclusively once the rupture front exits the high-stress plateau. Decreasing β sustains the rupture front over a longer distance after it exits the overstress zone, producing a higher peak moment rate, a longer STF duration, and a more gradual decay, while increasing β produces a shorter, more abrupt termination. Quantitatively, n_{decay} increases from 2.46 at $\beta = 18.75$ MPa/m to 4.12 at $\beta = 300$ MPa/m, confirming that β is a primary control on arrest-phase curvature. These results extend the earthquake arrest zone framework of Ke et al. (2021), which established that the initial stress distribution outside the overstress zone governs rupture termination, by demonstrating that this control is directly and quantitatively reflected in the STF arrest-phase shape, with β acting almost exclusively through the spatial extent of the arrest zone rather than through any modification of the growth phase. The distinction between abrupt and gradual arrest documented here is also relevant to near-fault ground motion hazard: recent observational work has identified a seismic stopping phase in near-field records of large strike-slip earthquakes that is generated most efficiently during abrupt rupture arrest (Kearse & Kaneko, 2026), suggesting that the arrest-phase curvature characterized by n_{decay} may have direct implications for stopping-phase amplitudes and near-fault ground motion. However, β alone cannot account for long-tailed STF shapes. Across the full range of β values examined here, n_{decay} remains at or above 2.46 and $\hat{t}_{\text{peak}}$ remains above 0.5, meaning that β produces only moderate variations in arrest-phase curvature and does not shift the STF peak toward the early-peaking asymmetry characteristic of long-tailed natural events.

4.3 Overstress zone geometry, confinement, and arrest

Overstress zone geometry exerts control on all three STF phases through two distinct mechanisms, with short-axis confinement governing plateau development during the growth and steady phases, and progressive area reduction in the tapered distal region governing arrest-phase duration and curvature.

For elongated rectangular overstress zones, rupture rapidly saturates along the short axis, limiting further increase in slipping area while sustained propagation along the long axis maintains an approximately steady moment-release rate. This width-saturated regime, in which the steady energy release rate becomes length-independent (Weng & Ampuero, 2019), produces the pronounced plateau observed at high aspect ratios and gives rise to pulse-like local slip histories even without an explicit healing mechanism in the friction law. Pulse-like rupture has been attributed to several distinct mechanisms in the literature, including velocity-weakening friction with restrengthening (Perrin et al., 1995; Zheng & Rice, 1998), rate-and-state friction with strong velocity dependence (Lapusta et al.,

2000), and fault heterogeneity (Lambert et al., 2021). In contrast to these frictional or structural origins, the pulse-like behavior documented here arises purely from geometric confinement of the overstress zone, without any modification of the friction law or fault properties. This geometric mechanism is most consistent with the observation that the pulse width scales directly with the short-axis width W rather than with any frictional length scale, and that the pulse-like character disappears at low aspect ratios where geometric confinement is absent. Edge initiation amplifies this effect by promoting unilateral propagation, producing a more clearly defined plateau and a more asymmetric STF relative to center initiation.

For pentagonal overstress zones, the progressively narrowing distal geometry forces the moment-release rate to decrease gradually as the rupture front advances into a region of shrinking available slipping area. This progressive area reduction produces a smoother and more prolonged arrest phase with smaller n_{decay}, demonstrating that arrest-phase duration and curvature can be modified by geometry alone, without any change in frictional parameters. However, as with β, geometric tapering alone cannot reproduce pronounced long-tailed STF shapes. Across the full range of L_2/W values examined here, the resulting STFs retain a trapezoidal shape with a steep, nearly identical rise and a plateau that transitions into a progressively more gradual decay, but the peak remains near or above the midpoint of the STF duration and the decay tail does not approach the strongly early-peaking, long-tailed asymmetry characteristic of natural earthquake STFs.

4.4 Frictional weakening, super-quadratic growth, and long-tailed arrest

Beyond geometry and stress distribution, the secondary weakening distance δ_{c2} in the BLSW law modulates both the growth and arrest phases of the STF. Increasing δ_{c2} prolongs the interval over which the fault remains in active weakening, reducing the peak moment rate, steepening the growth-phase curvature beyond the classical t^2 prediction, and producing a smoother, longer-tailed arrest phase.

A compact physical explanation for super-quadratic growth ($n_{\mathrm{rise}} > 2$) under bilinear weakening follows from the Zheng and Rice (1998) effective boundary condition,

$$\tau(x,z,t) \;=\; \tau_0 + \phi(x,z,t) \;-\; \frac{\mu}{2c}\,\dot{u}(x,z,t), \tag{4}$$

where u is the displacement of one side of the fault ($\delta = 2u$ for a fault embedded in a homogeneous elastic medium), $\dot{u}$ the particle velocity at the fault surface, τ is the instantaneous frictional resistance, τ_0 is the locked-fault shear stress level, ϕ is the elastic interaction term due to nonuniform slip, and $(\mu/2c)\dot{u}$ is the radiation-damping term. Defining the elastic driving stress as $\tau_{\mathrm{drive}}(x,z,t) \equiv \tau_0 + \phi(x,z,t)$, differentiating in time, and introducing the weakening rate $w(u) \equiv -d\tau/du > 0$, we obtain the central dynamic balance,

$$\frac{\mu}{2c}\,\ddot{u} \;=\; \dot{\tau}_{\mathrm{drive}} + w(u)\,\dot{u}. \tag{5}$$

Equation (5) shows that local re-acceleration ($\ddot{u} > 0$) can occur even when $\dot{\tau}_{\mathrm{drive}}$ is negative, so that as long as weakening persists ($w > 0$) and sliding continues ($\dot{u} > 0$), local velocity recovery can occur provided the weakening term $w\dot{u}$ is sufficiently large, a mechanism also reported in recent fully dynamic rupture simulations (Ferry & Molinari, 2025). This behavior is directly illustrated by the time histories of $\dot{\tau}_{\mathrm{drive}}$ and the weakening term $w\dot{u}$ at the same fault location for two values of δ_{c2} (Fig. 7), which confirm that a period of local slip re-acceleration occurs during the secondary weakening stage even as $\dot{\tau}_{\mathrm{drive}}$ remains negative.

For a bilinear law, the primary and secondary weakening slopes are $w_1 = 2(\tau_p - \tau_{r1})/\delta_{c1}$ and $w_2 = 2(\tau_{r1} - \tau_{r2})/(\delta_{c2} - \delta_{c1})$, where the factor of 2 arises because w is

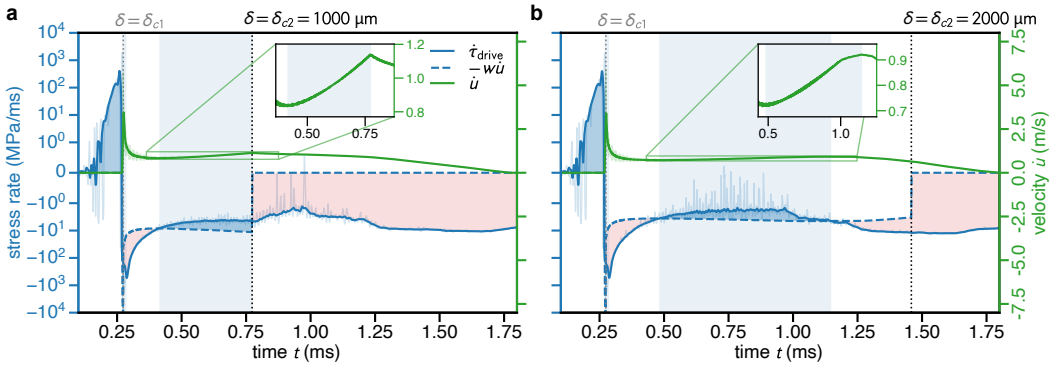


Figure 7: **Local stress rate and slip rate time histories illustrating the re-acceleration mechanism.** Time histories showing the elastic driving stress rate $\dot{\tau}_{\text{drive}}$ (blue solid), the weakening term $-w\dot{u}$ (blue dashed), and the local particle velocity $\dot{u}$ (green), recorded at the same fault location $(x, z) = (0.3, 0)$ m as the rupture front passes through, for (a) $\delta_{c2} = 1000$ µm and (b) $\delta_{c2} = 2000$ µm. Faint curves show the raw signals, and bold curves show their smoothed counterparts. Vertical dotted lines mark the instants when local slip reaches δ_{c1} and δ_{c2}, corresponding to the transition from the primary to the secondary weakening stage of the BLSW law and the end of weakening, respectively. The blue shaded regions between the curves indicate where $\dot{\tau}_{\text{drive}} > -w\dot{u}$, satisfying the condition for local slip re-acceleration ($\ddot{u} > 0$), while the pink shaded regions indicate where $\dot{\tau}_{\text{drive}} < -w\dot{u}$, corresponding to local slip deceleration ($\ddot{u} < 0$). The light blue vertical bands mark the resulting re-acceleration intervals, during which $\dot{u}$ recovers, as magnified in the insets. Note that re-acceleration occurs during the secondary weakening stage ($\delta_{c1} < \delta < \delta_{c2}$) despite $\dot{\tau}_{\text{drive}}$ being negative, confirming that the $w_2\dot{u}$ term is sufficient to satisfy $\dot{\tau}_{\text{drive}} > -w\dot{u}$ and drive local slip recovery. In (a), $\dot{u}$ recovers and peaks precisely when δ reaches δ_{c2}, whereas in (b) the recovery is weaker and terminates before δ reaches δ_{c2}. Once δ exceeds δ_{c2}, the weakening term drops to zero and the subsequent deceleration ($\ddot{u} < 0$) is irreversible.

defined with respect to $u = \delta/2$, so increasing δ_{c2} extends the duration of the $w_2 > 0$ regime but also reduces w_2 itself. These two effects compete. A longer secondary weakening stage allows a larger fraction of the fault area to satisfy $\dot{\tau}_{\text{drive}} + w\dot{u} > 0$ for longer, while a smaller w_2 weakens the very term that drives the recovery. This competition is directly visible in Fig. 7, where the local slip rate recovers more strongly at $\delta_{c2} = 1000$ µm than at $\delta_{c2} = 2000$ µm, and in the latter case the recovery terminates even before δ reaches δ_{c2}, as the weakened $w_2\dot{u}$ term can no longer offset the negative $\dot{\tau}_{\text{drive}}$. Upon spatial integration, local re-acceleration elevates the spatially averaged slip rate $\overline{V}(t)$ during the growth phase. Writing $\overline{V}(t) \sim t^{\gamma}$ over this interval gives $\dot{M}_0(t) \propto A(t)\,\overline{V}(t) \sim t^{2+\gamma}$, which naturally yields $n_{\text{rise}} = 2 + \gamma > 2$ in the STF fits. The exponent γ is not a free parameter but reflects the degree to which secondary weakening elevates the spatially averaged slip rate, and the competition between the duration and the rate of secondary weakening explains why n_{rise} peaks at $\delta_{c2} = 1000$ µm and decreases gradually as δ_{c2} increases to 2000 µm (Table S10). It is this re-acceleration during secondary weakening, rather than post-δ_{c2} behavior, that the fitted exponents measure in the super-quadratic regime; the fully weakened fraction of the slipping area ($\delta \geq \delta_{c2}$) reaches only about 10% at the 75% fitting bound for $\delta_{c2} = 1000$ µm, and remains zero throughout the rise for $\delta_{c2} = 2000$ µm (Fig. S10). At $\delta_{c2} = 500$ µm, by contrast, over three quarters of the slipping area has passed δ_{c2} by the fitting bound (Fig. S10), and the resulting mixing of decelerating area into the fitted rise plausibly depresses the exponent below the quadratic value, so the re-acceleration interpretation applies to the super-quadratic cases with $\delta_{c2} \geq$

1000 µm. The same prolonged weakening tail also smooths the arrest phase by sustaining non-negligible slip well after the rupture front has decelerated, producing the long-tailed decay documented here and in inversions of large earthquakes (Duputel et al., 2013; Li, 2022).

An alternative and complementary route to super-quadratic growth arises from fault heterogeneity rather than from the friction law. Ide and Aochi (2005) modeled earthquakes as cascading ruptures across a hierarchical population of patches with scale-dependent fracture energy, and Renou et al. (2022) showed that dynamic rupture simulations built on this multiscale framework generate transient moment-rate accelerations whose apparent growth exponent approaches the observed average of 2.7 (Renou et al., 2019) as rupture cascades from smaller to larger patches. The frequent observation of nearly identical onsets shared by co-located small and large earthquakes (Ide, 2019) suggests that such site-specific hierarchical patch structures are common in nature. Our results show that heterogeneity is not strictly required for super-quadratic growth, since a homogeneous fault governed by BLSW friction with an extended weakening tail also yields $n_{\mathrm{rise}} > 2$; the two mechanisms are not mutually exclusive, and in natural earthquakes cascade-up growth across heterogeneous patches and prolonged local weakening may well operate simultaneously. Secondary weakening is therefore sufficient but not necessary for super-quadratic growth, and our uniform-friction, single-patch configuration cannot distinguish between the two routes in natural events.

4.5 Scale-dependent breakdown and the origin of long-tailed STFs

A key finding that emerges from comparing the four mechanisms is that macroscale structural controls are insufficient on their own to reproduce long-tailed STF shapes. Even the pentagonal geometry, which was designed to impose a geometrically tapered arrest zone and force a gradual termination, produces only a moderately prolonged decay, as the arrest phase lengthens with increasing L_2/W but the STF tail remains relatively compact compared to the long-tailed decays documented in natural earthquake inversions (Duputel et al., 2013; Li, 2022). By contrast, a pronounced long tail emerges naturally once the BLSW friction law is introduced with a sufficiently large δ_{c2}. Critically, the cases that most closely reproduce the observed long-tailed behavior are those in which δ_{c2} is comparable to or exceeds the final slip accumulated within the overstress zone, meaning that a substantial fraction of the fault area has not yet completed the secondary weakening process by the time the rupture front arrests. This condition is directly analogous to the scale-dependent breakdown concept of Cocco et al. (2023), in which the breakdown work governing rupture arrest is set by a weakening process that operates over a length scale comparable to the total slip, rather than being exhausted early in the slip history. A broader framework for such scale-dependent energy dissipation is discussed in the context of fracture-mechanics analyses of earthquake energy budgets (Kammer et al., 2024). Our results therefore provide dynamic rupture simulation support for scale-dependent breakdown as a mechanism for generating the long-tailed STF shapes observed in large earthquakes, and suggest that the secondary weakening distance δ_{c2} is a physically meaningful parameter that encodes information about the operative slip-weakening scale at the source. Laboratory measurements add a complementary caution: apparent breakdown-work scaling can also arise from nonlocal elastic unloading of the surrounding system rather than from intrinsic fault weakening (Ke et al., 2026), so a large inferred breakdown work need not imply a large intrinsic weakening scale.

4.6 Coupled controls and implications for natural earthquakes

The four mechanisms examined here act on distinct STF features, with rupture initiation location governing growth-phase curvature and STF symmetry, geometric confinement controlling plateau development and duration, background stress gradient determining arrest-phase duration and curvature, and δ_{c2} modulating super-quadratic growth

acceleration and long-tailed decay. Combined simulations now test this separability directly. Varying the stress gradient at edge initiation leaves the growth phase edge-controlled while the arrest-phase control of β persists with a widened quantitative range (Section 3.2, Fig. S6, Table S11), and varying δ_{c2} at edge initiation preserves the re-acceleration mechanism, with n_{rise} rising to 1.64 at $\delta_{c2} = 1000$ µm on the nearly linear edge baseline while the weakening tail lengthens the arrest phase (Fig. S7, Table S12). The controls therefore remain largely separable under joint variation, and the wide diversity of STF shapes observed in natural earthquakes (Vallée & Douet, 2016; Meier et al., 2017; Renou et al., 2019) can be understood as arising from combinations of these mechanisms. The combinations are not strictly additive in every respect, however; in the combined edge and δ_{c2} suite the normalized peak time remains near 0.56 to 0.59 rather than shifting toward the early-peaking values suggested by superposing the single-mechanism trends, so the strongly early-peaking, long-tailed shapes documented in earthquake catalogs are not reproduced by this combination alone. The shape families documented here characterize the systematic component of this diversity; reproducing the magnitude-independent residual dispersion of Meier et al. (2017) would require ensemble variation of initiation location, geometry, and friction parameters across events, which we leave to future work. These results suggest that STF shape carries recoverable information about the physical state of the fault at the time of rupture, including its geometry, stress environment, and frictional properties, with direct implications for seismic source inversion and near-fault ground motion prediction.

4.7 Limitations and outlook

The present study provides a systematic framework for understanding how four physical mechanisms govern STF shape, but several important limitations should be acknowledged.

All simulations adopt the earthquake arrest zone stress distribution of Ke et al. (2021), in which the overstress zone is surrounded by a smooth, radially decaying stress gradient. This configuration is an idealized and deliberately simplified representation of stress heterogeneity, inspired by stress measurements from large-scale laboratory earthquake experiments (Ke et al., 2018, 2021), and is intended to isolate the effect of the arrest zone geometry in a controlled setting. Isolating a single overstressed patch is likewise a deliberate modeling choice made to expose mechanism-level controls, not a claim about natural fault structure. Natural faults are subject to heterogeneity in stress and strength at multiple scales (Lapusta et al., 2000; Lambert et al., 2021; Ide, 2019), which can produce irregular moment-rate histories, multiple sub-event peaks, and complex arrest patterns that are not captured by the smooth, single-peaked STFs produced here. Incorporating more realistic stress heterogeneity would likely broaden the range of STF shapes that can be generated by the structural controls alone, potentially reducing the requirement for large δ_{c2} to reproduce long-tailed behavior. In particular, the late breaking of small asperities triggered by the main rupture provides a natural alternative mechanism for long-tailed STFs that does not invoke the shape of the friction law, echoing classical barrier and asperity models in which rupture through heterogeneous fault strength radiates complex, multi-pulse moment release (Das & Aki, 1977; Das & Kostrov, 1983). Subevent decompositions of global STF catalogs indicate that most large earthquakes comprise multiple subevents (Danré et al., 2019), and long-tailed moment-rate functions are indeed a common feature of multisubevent earthquakes (Liu et al., 2023). The secondary weakening distance δ_{c2} is therefore sufficient, but not necessary, for generating long-tailed STF shapes. Heterogeneity off the fault plane can add further complexity to the moment rate. Mature faults are commonly bordered by low-velocity damage zones (Ben-Zion & Sammis, 2003), within which ruptures develop oscillatory rupture speeds modulated by waves reflected inside the zone (Harris & Day, 1997) and by head waves traveling along its interfaces (Huang et al., 2014), and can shift toward pulse-like propagation styles (Idini & Ampuero, 2020), imprinting moment-rate fluctuations that our

homogeneous-medium simulations cannot produce. Because these fluctuation periods scale with the wave travel time across the damage zone, they are short compared with the growth, plateau, and arrest phases analyzed here. Fault roughness likewise generates continuous rupture-speed fluctuations and bursts of high-frequency radiation on geometrically heterogeneous faults (Dunham et al., 2011). Discriminating between frictional and heterogeneity-based origins of long tails in natural earthquakes will require analyses that resolve subevent structure within individual STFs.

The present simulations also assume that friction follows either LSW or BLSW uniformly across the entire fault surface. Natural faults likely exhibit spatially variable frictional properties, and more complex weakening laws, including rate-and-state friction (Lapusta et al., 2000), flash heating (Rice, 2006; Goldsby & Tullis, 2011), or thermally activated mechanisms (Viesca & Garagash, 2015), may produce STF shapes that differ systematically from those documented here. In particular, velocity-weakening friction with restrengthening can produce self-healing pulses (Perrin et al., 1995; Zheng & Rice, 1998) through a mechanism distinct from the geometric confinement identified here, and the interplay between these two pulse-generating mechanisms remains to be explored.

More broadly, the four mechanisms examined here do not exhaust the full parameter space of controls on STF shape. Factors not examined in this study include, to name a few, off-fault damage and inelasticity (Andrews, 2005; De Paola et al., 2025), dynamic pore pressure changes (Rice, 2006; Gori et al., 2021), and the three-dimensional geometry of the seismogenic zone (Tinti, 2005; Sato et al., 2026). Each of these could independently modify the growth, steady, or arrest phase of the STF in ways that are not captured by the present framework.

Despite these limitations, the quantitative metrics introduced here, namely n_{rise}, n_{decay}, and $\hat{t}_{\mathrm{peak}}$, are designed to be directly comparable with observed STF catalogs (Vallée & Douet, 2016), and a systematic test of the simulated shape families against such catalogs is a principal direction for future work, alongside simulation studies that progressively relax the idealizations adopted here.

5 Conclusions

We have conducted systematic dynamic rupture simulations to quantify how four physical mechanisms, namely rupture initiation location, background stress gradient β, overstress zone geometry, and secondary slip-weakening distance δ_{c2}, individually and collectively govern the shape of the source time function across its growth, steady, and arrest phases. By varying each mechanism independently and characterizing the resulting STF shapes using the growth-phase curvature exponent n_{rise}, the arrest-phase curvature exponent n_{decay}, and the normalized peak time $\hat{t}_{\mathrm{peak}}$, we establish the following conclusions.

Rupture initiation location is the primary control on growth-phase curvature and STF symmetry. Center initiation within a circular overstress zone produces a nearly parabolic STF with $n_{\mathrm{rise}} \approx 2$ and $\hat{t}_{\mathrm{peak}} \approx 0.5$, consistent with classical self-similar bilateral rupture expansion, whereas progressive offset toward the overstress zone boundary shifts the growth phase from quadratic to nearly linear and delays $\hat{t}_{\mathrm{peak}}$ from 0.52 to 0.62, reproducing the asymmetric STF shapes associated with unilateral and edge-nucleated ruptures.

The background stress gradient β acts almost exclusively on the arrest phase, leaving the growth phase unaffected by construction for centered initiation and only mildly modified for edge initiation. Increasing β from 18.75 to 300 MPa/m raises n_{decay} from 2.46 to 4.12 and reduces the total STF duration from 1.21 to 0.87 ms, demonstrating that β is a quantifiable and independent control on arrest-phase curvature operating through the spatial extent of the arrest zone.

Overstress zone geometry governs plateau development and arrest-phase character through two distinct mechanisms. Short-axis confinement in elongated rectangular zones produces a quasi-steady plateau and pulse-like slip histories without any explicit self-healing mechanism in the friction law, while progressive area reduction in pentagonal zones produces smoother and more prolonged arrest phases. Neither geometric confinement nor stress gradient alone, however, can reproduce strongly early-peaking, long-tailed STF shapes.

The secondary weakening distance δ_{c2} is the only mechanism among those examined here that is capable of producing pronounced long-tailed STF shapes. Increasing δ_{c2} prolongs the interval of active fault weakening, steepening the growth-phase curvature beyond the classical t^2 prediction through a local re-acceleration mechanism, and producing progressively smoother, longer-tailed arrest phases. The cases that most closely reproduce observed long-tailed STFs are those in which δ_{c2} is comparable to or exceeds the total fault slip, consistent with the scale-dependent breakdown framework in which breakdown work is governed by a weakening process operating over a length scale comparable to the total slip.

These four mechanisms act on largely separable features of the STF, and combined simulations confirm that the separability largely persists under joint variation, with mild and quantified coupling and one clear departure from additivity in peak timing. Much of the wide diversity of STF shapes observed in natural earthquakes can be understood as arising from combinations of these mechanisms operating alongside heterogeneity-based processes not examined here, and the quantitative metrics n_{rise}, n_{decay}, and $\hat{t}_{\mathrm{peak}}$ introduced here provide a systematic framework for connecting dynamic rupture simulations to observed STF catalogs.

Open Research Section

All simulations use version 0.9 of the UGUCA spectral boundary-integral code (Kammer et al., 2021a, 2021b), which is openly available under the LGPL-3.0 license at `https://gitlab.com/uguca/uguca`. The simulation source code, input files, STF time series, extracted metrics, and plotting scripts for all simulation cases presented in this study are openly available in the Zenodo repository at `https://doi.org/10.5281/zenodo.22009178` (Wang & Ke, 2026). Extracted STF shape metrics for all simulation cases are provided in Tables S1–S12 of the Supporting Information.

Acknowledgments

This work was supported by the National Science and Technology Council, Taiwan (NSTC 113-2116-M-002-031-MY3) and the Yushan Fellow Program of the Ministry of Education, Taiwan (MOE-113-YSFEE-0003-003-P1). C.-Y. K. gratefully acknowledges support from the Garmin Scholar Program at National Taiwan University, funded by the Kao Family Foundation. The successful completion of this research was made possible by the academic resources and advanced research infrastructure provided by the National Center for High-Performance Computing, National Institutes of Applied Research (NIAR), Taiwan. We gratefully acknowledge their invaluable support. We thank Editor Satoshi Ide, Associate Editor Yihe Huang, and two anonymous reviewers for their thoughtful and constructive comments, which substantially improved this manuscript. AI assistants (Claude, Anthropic; Codex, OpenAI) were used to assist with code and the preparation of this manuscript; the authors reviewed and verified all content and take full responsibility for it.

Conflict of Interest

The authors declare no conflicts of interest relevant to this study.

References

Andrews, D. J. (1976a). Rupture propagation with finite stress in antiplane strain. *Journal of Geophysical Research*, *81*(20), 3575–3582. doi: 10.1029/JB081i020p03575

Andrews, D. J. (1976b). Rupture velocity of plane strain shear cracks. *Journal of Geophysical Research*, *81*(32), 5679–5687. doi: 10.1029/JB081i032p05679

Andrews, D. J. (2005). Rupture dynamics with energy loss outside the slip zone. *Journal of Geophysical Research*, *110*(B1), B01307. doi: 10.1029/2004JB003191

Bažant, Z. P. (2004). Scaling theory for quasibrittle structural failure. *Proceedings of the National Academy of Sciences*, *101*(37), 13400–13407. doi: 10.1073/pnas.0404096101

Ben-Zion, Y., & Sammis, C. G. (2003). Characterization of Fault Zones. *Pure and Applied Geophysics*, *160*(3), 677–715. doi: 10.1007/PL00012554

Breitenfeld, M. S., & Geubelle, P. H. (1998). Numerical analysis of dynamic debonding under 2D in-plane and 3D loading. *International Journal of Fracture*, *93*(1/4), 13–38. doi: 10.1023/A:1007535703095

Cebry, S. B. L., Ke, C.-Y., & McLaskey, G. C. (2022). The Role of Background Stress State in Fluid-Induced Aseismic Slip and Dynamic Rupture on a 3-m Laboratory Fault. *Journal of Geophysical Research: Solid Earth*, *127*(8), e2022JB024371. doi: 10.1029/2022JB024371

Cebry, S. B. L., Ke, C.-Y., Shreedharan, S., Marone, C., Kammer, D. S., & McLaskey, G. C. (2022). Creep fronts and complexity in laboratory earthquake sequences illuminate delayed earthquake triggering. *Nature Communications*, *13*(1), 6839. doi: 10.1038/s41467-022-34397-0

Chu, R., Zhu, L., & Helmberger, D. V. (2009). Determination of earthquake focal depths and source time functions in central Asia using teleseismic *P* waveforms. *Geophysical Research Letters*, *36*(17), 2009GL039494. doi: 10.1029/2009GL039494

Cocco, M., Aretusini, S., Cornelio, C., Nielsen, S. B., Spagnuolo, E., Tinti, E., & Di Toro, G. (2023). Fracture Energy and Breakdown Work During Earthquakes. *Annual Review of Earth and Planetary Sciences*, *51*(1), 217–252. doi: 10.1146/annurev-earth-071822-100304

Danré, P., Yin, J., Lipovsky, B. P., & Denolle, M. A. (2019). Earthquakes Within Earthquakes: Patterns in Rupture Complexity. *Geophysical Research Letters*, *46*(13), 7352–7360. doi: 10.1029/2019GL083093

Das, S., & Aki, K. (1977). Fault plane with barriers: A versatile earthquake model. *Journal of Geophysical Research*, *82*(36), 5658–5670. doi: 10.1029/JB082i036p05658

Das, S., & Kostrov, B. V. (1983). Breaking of a single asperity: Rupture process and seismic radiation. *Journal of Geophysical Research: Solid Earth*, *88*(B5), 4277–4288. doi: 10.1029/JB088iB05p04277

Das, S., & Kostrov, B. V. (1988). An investigation of the complexity of the earthquake source time function using dynamic faulting models. *Journal of Geophysical Research: Solid Earth*, *93*(B7), 8035–8050. doi: 10.1029/JB093iB07p08035

Denolle, M. A. (2019). Energetic Onset of Earthquakes. *Geophysical Research Letters*, *46*(5), 2458–2466. doi: 10.1029/2018GL080687

De Paola, N., Bullock, R. J., Holdsworth, R. E., Marco, S., & Nielsen, S. (2025). Off-fault damage controls near-surface rupture behaviour in soft sediments. *Nature Communications*, *16*(1), 11295. doi: 10.1038/s41467-025-66467-4

Dunham, E. M., Belanger, D., Cong, L., & Kozdon, J. E. (2011). Earthquake Ruptures with Strongly Rate-Weakening Friction and Off-Fault Plasticity, Part 2: Nonplanar Faults. *Bulletin of the Seismological Society of America*, *101*(5), 2308–2322. doi: 10.1785/0120100076

Duputel, Z., Tsai, V. C., Rivera, L., & Kanamori, H. (2013). Using centroid time-delays to characterize source durations and identify earthquakes with unique characteristics. *Earth and Planetary Science Letters*, *374*, 92–100. doi: 10.1016/j.epsl.2013.05.024

Ferry, R., & Molinari, J.-F. (2025). Do slip-weakening laws shapes influence rupture dynamics? *Extreme Mechanics Letters*, *74*, 102272. doi: 10.1016/j.eml.2024.102272

Geubelle, P. H., & Rice, J. R. (1995). A spectral method for three-dimensional elastodynamic fracture problems. *Journal of the Mechanics and Physics of Solids*, *43*(11), 1791–1824. doi: 10.1016/0022-5096(95)00043-I

Goldsby, D. L., & Tullis, T. E. (2011). Flash Heating Leads to Low Frictional Strength of Crustal Rocks at Earthquake Slip Rates. *Science*, *334*(6053), 216–218. doi: 10.1126/science.1207902

Gori, M., Rubino, V., Rosakis, A. J., & Lapusta, N. (2021). Dynamic rupture initiation and propagation in a fluid-injection laboratory setup with diagnostics across multiple temporal scales. *Proceedings of the National Academy of Sciences*, *118*(51), e2023433118. doi: 10.1073/pnas.2023433118

Harris, R. A., & Day, S. M. (1997). Effects of a low-velocity zone on a dynamic rupture. *Bulletin of the Seismological Society of America*, *87*(5), 1267–1280. doi: 10.1785/BSSA0870051267

Heaton, T. H. (1990). Evidence for and implications of self-healing pulses of slip in earthquake rupture. *Physics of the Earth and Planetary Interiors*, *64*(1), 1–20. doi: 10.1016/0031-9201(90)90002-F

Hirano, S. (2022). Source time functions of earthquakes based on a stochastic differential equation. *Scientific Reports*, *12*(1), 3936. doi: 10.1038/s41598-022-07873-2

Houston, H. (2001). Influence of depth, focal mechanism, and tectonic setting on the shape and duration of earthquake source time functions. *Journal of Geophysical Research: Solid Earth*, *106*(B6), 11137–11150. doi: 10.1029/2000JB900468

Huang, Y., Ampuero, J.-P., & Helmberger, D. V. (2014). Earthquake ruptures modulated by waves in damaged fault zones. *Journal of Geophysical Research: Solid Earth*, *119*(4), 3133–3154. doi: 10.1002/2013JB010724

Ida, Y. (1972). Cohesive force across the tip of a longitudinal-shear crack and Griffith's specific surface energy. *Journal of Geophysical Research*, *77*(20), 3796–3805. doi: 10.1029/JB077i020p03796

Ide, S. (2019). Frequent observations of identical onsets of large and small earthquakes. *Nature*, *573*(7772), 112–116. doi: 10.1038/s41586-019-1508-5

Ide, S., & Aochi, H. (2005). Earthquakes as multiscale dynamic ruptures with heterogeneous fracture surface energy. *Journal of Geophysical Research: Solid Earth*, *110*(B11), B11303. doi: 10.1029/2004JB003591

Idini, B., & Ampuero, J.-P. (2020). Fault-Zone Damage Promotes Pulse-Like Rupture and Back-Propagating Fronts via Quasi-Static Effects. *Geophysical Research Letters*, *47*(23), e2020GL090736. doi: 10.1029/2020GL090736

Jiang, J., & Lapusta, N. (2016). Deeper penetration of large earthquakes on seismically quiescent faults. *Science*, *352*(6291), 1293–1297. doi: 10.1126/science.aaf1496

Kammer, D. S., Albertini, G., & Ke, C.-Y. (2021a). UGUCA: A spectral-boundary-integral method for modeling fracture and friction. *SoftwareX*, *15*, 100785. doi: 10.1016/j.softx.2021.100785

Kammer, D. S., Albertini, G., & Ke, C.-Y. (2021b). *UGUCA* (Version 0.9) [Software]. GitLab. https://gitlab.com/uguca/uguca/-/releases/v0.9

Kammer, D. S., McLaskey, G. C., Abercrombie, R. E., Ampuero, J.-P., Cattania, C., Cocco, M., ... Tinti, E. (2024). Earthquake energy dissipation in a fracture mechanics framework. *Nature Communications*, *15*(1), 4736. doi:

10.1038/s41467-024-47970-6

Ke, C.-Y., Chang, G. T., McLaskey, G. C., Kammer, D. S., & Marone, C. (2026). Nonlocal elastic unloading as a mechanism for breakdown work scaling in laboratory earthquakes. *Earth and Planetary Science Letters*, *693*, 120283. doi: 10.1016/j.epsl.2026.120283

Ke, C.-Y., McLaskey, G. C., & Kammer, D. S. (2018). Rupture Termination in Laboratory-Generated Earthquakes. *Geophysical Research Letters*, *45*(23), 12784–12792. doi: 10.1029/2018GL080492

Ke, C.-Y., McLaskey, G. C., & Kammer, D. S. (2021). The earthquake arrest zone. *Geophysical Journal International*, *224*(1), 581–589. doi: 10.1093/gji/ggaa386

Ke, C.-Y., McLaskey, G. C., & Kammer, D. S. (2022). Earthquake breakdown energy scaling despite constant fracture energy. *Nature Communications*, *13*(1), 1005. doi: 10.1038/s41467-022-28647-4

Kearse, J., & Kaneko, Y. (2026). Stopping phase reveals abrupt arrest of large strike-slip earthquakes. *Science*, *392*(6801), 946–950. doi: 10.1126/science.aef3733

Lambert, V., Lapusta, N., & Perry, S. M. (2021). Propagation of large earthquakes as self-healing pulses or mild cracks. *Nature*, *591*(7849), 252–258. doi: 10.1038/s41586-021-03248-1

Lapusta, N., Rice, J. R., Ben-Zion, Y., & Zheng, G. (2000). Elastodynamic analysis for slow tectonic loading with spontaneous rupture episodes on faults with rate- and state-dependent friction. *Journal of Geophysical Research: Solid Earth*, *105*(B10), 23765–23789. doi: 10.1029/2000JB900250

Li, Z. (2022). A Generic Model of Global Earthquake Rupture Characteristics Revealed by Machine Learning. *Geophysical Research Letters*, *49*(8), e2021GL096464. doi: 10.1029/2021GL096464

Liu, M., Huang, Y., & Ritsema, J. (2023). Characterizing Multisubevent Earthquakes Using the Brune Source Model. *Bulletin of the Seismological Society of America*, *113*(2), 577–591. doi: 10.1785/0120220192

Madariaga, R. (1976). Dynamics of an expanding circular fault. *Bulletin of the Seismological Society of America*, *66*(3), 639–666. doi: 10.1785/BSSA0660030639

McLaskey, G. C., Kilgore, B. D., & Beeler, N. M. (2015). Slip-pulse rupture behavior on a 2 m granite fault. *Geophysical Research Letters*, *42*(17), 7039–7045. doi: 10.1002/2015GL065207

Meier, M.-A., Ampuero, J.-P., & Heaton, T. H. (2017). The hidden simplicity of subduction megathrust earthquakes. *Science*, *357*(6357), 1277–1281. doi: 10.1126/science.aan5643

Meier, M.-A., Heaton, T., & Clinton, J. (2016). Evidence for universal earthquake rupture initiation behavior. *Geophysical Research Letters*, *43*(15), 7991–7996. doi: 10.1002/2016GL070081

Miyake, H. (2003). Source Characterization for Broadband Ground-Motion Simulation: Kinematic Heterogeneous Source Model and Strong Motion Generation Area. *Bulletin of the Seismological Society of America*, *93*(6), 2531–2545. doi: 10.1785/0120020183

Noda, S., & Ellsworth, W. L. (2016). Scaling relation between earthquake magnitude and the departure time from P wave similar growth. *Geophysical Research Letters*, *43*(17), 9053–9060. doi: 10.1002/2016GL070069

Okubo, K., Yamashita, F., & Fukuyama, E. (2026). Dynamics of non-self-similar earthquakes illuminated by a controlled fault asperity. *Nature Communications*, *17*(1), 3860. doi: 10.1038/s41467-026-72217-x

Paglialunga, F., Passelègue, F. X., Brantut, N., Barras, F., Lebihain, M., & Violay, M. (2022). On the scale dependence in the dynamics of frictional rupture: Constant fracture energy versus size-dependent breakdown work. *Earth and Planetary Science Letters*, *584*, 117442. doi: 10.1016/j.epsl.2022.117442

Palmer, A. C., & Rice, J. R. (1973). The Growth of Slip Surfaces in the Progressive Failure of Over-Consolidated Clay. *Proceedings of the Royal Society A: Mathematical, Physical and Engineering Sciences*, *332*(1591), 527–548. doi: 10.1098/rspa.1973.0040

Perrin, G., Rice, J. R., & Zheng, G. (1995). Self-healing slip pulse on a frictional surface. *Journal of the Mechanics and Physics of Solids*, *43*(9), 1461–1495. doi: 10.1016/0022-5096(95)00036-I

Pomyalov, A., Lubomirsky, Y., Braverman, L., Brener, E. A., & Bouchbinder, E. (2023). Self-healing solitonic slip pulses in frictional systems. *Physical Review E*, *107*(1), L013001. doi: 10.1103/PhysRevE.107.L013001

Reches, Z., & Fineberg, J. (2023). Earthquakes as Dynamic Fracture Phenomena. *Journal of Geophysical Research: Solid Earth*, *128*(3), e2022JB026295. doi: 10.1029/2022JB026295

Renou, J., Vallée, M., & Aochi, H. (2022). Deciphering the Origins of Transient Seismic Moment Accelerations by Realistic Dynamic Rupture Simulations. *Bulletin of the Seismological Society of America*, *112*(3), 1240–1251. doi: 10.1785/0120210221

Renou, J., Vallée, M., & Dublanchet, P. (2019). How Does Seismic Rupture Accelerate? Observational Insights From Earthquake Source Time Functions. *Journal of Geophysical Research: Solid Earth*, *124*(8), 8942–8952. doi: 10.1029/2019JB018045

Rice, J. R. (2006). Heating and weakening of faults during earthquake slip. *Journal of Geophysical Research: Solid Earth*, *111*(5), B05311. doi: 10.1029/2005JB004006

Sato, D. S. K., Yagi, Y., Okuwaki, R., & Fukahata, Y. (2026). Smooth surface reconstruction of earthquake faults from distributed moment-potency-tensor solutions. *Geophysical Journal International*, *245*(3), ggag116. doi: 10.1093/gji/ggag116

Scholz, C. H. (1998). Earthquakes and friction laws. *Nature*, *391*(6662), 37–42. doi: 10.1038/34097

Smith-Konter, B. R., Sandwell, D. T., & Shearer, P. (2011). Locking depths estimated from geodesy and seismology along the San Andreas Fault System: Implications for seismic moment release. *Journal of Geophysical Research*, *116*(B6), B06401. doi: 10.1029/2010JB008117

Tinti, E. (2005). A Kinematic Source-Time Function Compatible with Earthquake Dynamics. *Bulletin of the Seismological Society of America*, *95*(4), 1211–1223. doi: 10.1785/0120040177

Tocheport, A., Rivera, L., & Chevrot, S. (2007). A systematic study of source time functions and moment tensors of intermediate and deep earthquakes. *Journal of Geophysical Research: Solid Earth*, *112*(B7), 2006JB004534. doi: 10.1029/2006JB004534

Uenishi, K., & Rice, J. R. (2003). Universal nucleation length for slip-weakening rupture instability under nonuniform fault loading. *Journal of Geophysical Research: Solid Earth*, *108*(B1), 2042. doi: 10.1029/2001JB001681

Vallée, M. (2013). Source time function properties indicate a strain drop independent of earthquake depth and magnitude. *Nature Communications*, *4*(1), 2606. doi: 10.1038/ncomms3606

Vallée, M., & Douet, V. (2016). A new database of source time functions (STFs) extracted from the SCARDEC method. *Physics of the Earth and Planetary Interiors*, *257*, 149–157. doi: 10.1016/j.pepi.2016.05.012

Viesca, R. C., & Garagash, D. I. (2015). Ubiquitous weakening of faults due to thermal pressurization. *Nature Geoscience*, *8*(11), 875–879. doi: 10.1038/ngeo2554

Wang, C.-Y., & Ke, C.-Y. (2026). *Data and code for: Physical controls on the shape of earthquake source time functions* (Version 1.0.0) [Dataset]. Zenodo. doi: 10

.5281/zenodo.22009178

Weng, H., & Ampuero, J.-P. (2019). The Dynamics of Elongated Earthquake Ruptures. *Journal of Geophysical Research: Solid Earth*, *124*(8), 8584–8610. doi: 10.1029/2019JB017684

Wesnousky, S. G. (2006). Predicting the endpoints of earthquake ruptures. *Nature*, *444*(7117), 358–360. doi: 10.1038/nature05275

Zheng, G., & Rice, J. R. (1998). Conditions under which velocity-weakening friction allows a self-healing versus a cracklike mode of rupture. *Bulletin of the Seismological Society of America*, *88*(6), 1466–1483. doi: 10.1785/BSSA0880061466